PAPER

Check for updates

Two-dimensional SnO₂ anchored biomass-derived carbon nanosheet anode for high-performance Li-ion capacitors†

Chang Liu,‡[a] Zeyin He,‡[a] Jianmin Niu,[b] Qiang Cheng, [ID][a] Zongchen Zhao,[a] Haoran Li,[a] Jing Shi [ID] *[a] and Huanlei Wang [ID] *[a]

Lithium-ion capacitors (LICs) combine the advantages of both batteries and supercapacitors; they have attracted intensive attention among energy conversion and storage fields, and one of the key points of their research is the exploration of suitable battery-type electrode materials. Herein, a simple and low-cost strategy is proposed, in which SnO_2 particles are anchored on the conductive porous carbon nano-sheets (PCN) derived from coffee grounds. This method can inhibit the grain coarsening of Sn and the volume change of SnO_2 effectively, thus improving the electrochemical reversibility of the materials. In the lithium half cell (0–3.0 V *vs.* Li/Li⁺), the as-prepared SnO_2/PCN electrode yields a reversible capacity of 799 mA h g⁻¹ at 0.1 A g⁻¹ and decent long-term cyclability of 313 mA h g⁻¹ at 1 A g⁻¹ after 500 cycles. The excellent Li⁺ storage performance of SnO_2/PCN is beneficial from the hierarchical structure as well as the robust carbonaceous buffer layer. Besides, a LIC hybrid device with the as-prepared SnO_2/PCN anode exhibits outstanding energy and power density of 138 W h kg⁻¹ and 53 kW kg⁻¹ at a voltage window of 1.0–4.0 V. These promising results open up a new way to develop advanced anode materials with high rate and long life.

1. Introduction

With the development of new energy vehicles and intelligent wearable devices, people have higher requirements for electrochemical energy storage devices. At present, lithium-ion batteries (LIBs) and electrochemical capacitors (ECs) are widely used. The high energy density and high working voltage of LIBs make them competitive in portable electronic devices. However, its power density and cycle performance are less than desirable. Compared with LIBs, ECs possess the merits of high power density, superfast charge/discharge process and excellent cycle performance, and have been widely used in electric starting equipment. However, their energy density is too low, only about 1/10 of LIBs.[1,2] LICs are composed of a battery-type anode and a capacitor-type cathode, which integrate the advantages of both LIBs and ECs. As a technological innovation, they have solved the above problems and deliver high energy/power density.[3,4]

For the capacitor-type cathode, the charge storage mechanism is the adsorption/desorption process of ions, the specific capacity of cathode can be enhanced by enlarging surface areas and designing suitable pore distribution.[5] Therefore, carbon materials including carbon nanotubes, graphene and porous carbon *etc.* are preferred in LICs as capacitor-type cathode owning to their high SSA (more than 1000 m² g⁻¹), good electrical conductivity and excellent electrolyte accessibility. Current researches mainly focus on two aspects: one is the preparation of carbon materials with special morphology and multi-pore size, which is beneficial to accelerate ion transportation.[6,7] The other is surface functionalization, such as nitrogen-containing groups, which helps to improve the Faraday capacitance and the conductivity, and offer numerous active sites for lithium storage.[8–10]

Recently, biomass-derived carbon materials stand out due to their low cost and unique precursor structure.[11–13] More importantly, functionalized carbons can be directly prepared by them because of the inherent composition of the precursors, and they are beneficial to the reversible capacity of the electrodes. Shang *et al.* prepared sheet-like porous carbon with SSA up to 3577 m² g⁻¹ and well-defined micro/mesopore distributions using KOH as pore forming agent and walnut shell as precursor.[14] Jin *et al.* tailored B, N co-doped carbon nanosheets using H_3BO_3 as template by the hydrogen bond reaction between gelatin molecule and H_3BO_3,[15] which provided a capacity of 309 mA h g⁻¹ at 0.2 A g⁻¹ for 200 cycles. Gao *et al.*

ᵃSchool of Materials Science and Engineering, Ocean University of China, Qingdao 266100, People's Republic of China. E-mail: shijing@ouc.edu.cn; huanleiwang@gmail.com

ᵇShanghai Shipbuilding Technology Research Institute, No. 851, Zhongshan South 2nd Road, Xuhui District, Shanghai 200032, China

† Electronic supplementary information (ESI) available. See DOI: 10.1039/d1ra00822f

‡ These authors contributed equally to this work.

took advantage of amino/hydroxyl group in chitosan to chelate with metal ions and prepared a high content nitrogen doped (7.42 wt%) hierarchically porous carbon aerogel.[16] Abundant mesopores were boosted by Zn^{2+} evaporation in high temperature, which were beneficial to electrolyte impregnation and ion transportation.

For the battery-type anode, the charge storage depends on the intercalation/de-intercalation of lithium ions and the pseudocapacitance reaction.[17] In view of this kinetic imbalance between sluggish faradic reactions and relatively fast ion adsorption/desorption, the selection of appropriate battery-type electrode is of critical importance to improve the power density of LICs. Transition metal oxides (TMOs) such as SnO_2,[18] TiO_2,[3] Nb_2O_5,[19] MnO_2,[20] V_2O_5 [21] *etc.*, are considered to be excellent LICs anode materials. Among these, SnO_2 stands out since its high theoretical specific capacity (1494 mA h g^{-1} for lithium storage) as well as safe working voltage range (≈ 1.0 V *vs.* Li/Li$^+$). However, like most transition metal oxides, SnO_2 has poor conductivity and suffers from dramatic volume change during charge/discharge process, easy pulverization and agglomeration, which directly affects its cycling performance.[22–25] One of the common strategies to tackle these problems is to composite SnO_2 with conductive nano-materials, including carbon layer,[26,27] carbon nanotubes (CNTs)[28,29] and graphene[30,31] *etc.* For example, Cheng and co-workers dispersed SnO_2 quantum dots (≈ 5 nm) in a nitrogen-doped porous carbon matrix, the carbon matrix was used as a protective medium to stabilize structural changes. Meanwhile, the size of SnO_2/NC nanoclusters was adjusted. The modified SnO_2/NC exhibited high discharge capacity of 213 mA h g^{-1} at 1 A g^{-1} after 3000 cycles for sodium storage.[27] Gao *et al.*[32] restricted the growth of SnO_2 through filling SnO_2 nanoparticles into the micropores of MOF and introduced graphene to further enhance the electrical conductivity. The SnO_2@MOF/graphene showed a stable cycle performance of 450 mA h g^{-1} at 1 A g^{-1} after 1000 loops. However, the research on the storage performance of SnO_2-based biomaterials is limited.[33,34]

In this work, we demonstrate a facile preparation scheme for LICs fabricated with waste coffee grounds derived PCN cathode and SnO_2/PCN composite anode. The prepared PCN exhibits high specific surface area, multi-pore size distribution and excellent electrochemical performance, has a price advantage over graphene. Besides, PCN not only limits the agglomeration and pulverization of SnO_2 as a carbon matrix network and enhances the conductivity, but also synergizes with SnO_2 nanoparticles to enhance the electrochemical performance as the anode material. The fabricated SnO_2/PCN//PCN delivers a maximum energy and power output of 138 W h kg^{-1} and 53 kW kg^{-1}. It shows that LICs with both high-power density and energy density can be obtained, and its environmental friendliness and price advantages make it a potential material in high-performance energy storage device for large-scale production.

2. Experimental section

2.1. Synthesis of PCN

PCN was prepared by waste coffee grounds (WCGs) obtained from espresso roast coffee beans (Starbucks®, commercial beverage manufacturers). Firstly, 3 g WCGs were dried at 80 °C for 48 h to evaporate the residual water and dissolved in 50 mL deionized water. The mixture was transferred to a Teflon autoclave, the reactor was placed in an oven and heated up to 180 °C for 12 h. Secondly, the as-prepared precursor (1 g) was mixed with 50 mL KOH as activating agent and stirred for 24 h, then dried at 80 °C. The precursor was carbonized at 1000 °C under nitrogen flow for 1 h. Finally, PCN was obtained after washing with 2 M HCl for 24 h and deionized water repeatedly, followed by filtering and drying.

2.2. Synthesis of SnO₂/PCN nanocomposites

SnO_2/PCN composite was prepared as follows: 1 g PCN was treated with 50 wt% HNO_3 and held for 6 h, then 20 mg the above product, 70 mg $SnCl_4 \cdot 5H_2O$ and 40 mg $Na_2S_2O_3$ were dispersed in 20 mL deionized water with violent stirring. After that, a certain amount of $NH_3 \cdot H_2O$ was added to the above suspension until the pH reached 6 and kept evaporation at 80 °C under oil bath condition. The final product was then extracted with ethanol and dried overnight. For comparison, pure SnO_2 was synthesized by the above-mentioned procedures under the same experimental conditions without adding any PCN.

2.3. Material characterization

X-ray diffraction (XRD) was recorded by a D8 ADVANCE with Cu Kα radiation to investigate the phase crystallinity and composition. Scanning Electron Microscope (SEM, Sigma HD), transmission electron microscopy (TEM, FEI TF20) were conducted to characterize the morphology and microstructure of SnO_2, PCN and SnO_2/PCN, respectively. Raman spectra were obtained by utilizing a laser wavelength of 514 nm on HORIBA Lab RAM HR Raman Evolution spectrometer. The X-ray photoelectron spectroscopy (XPS) measurements were taken on Thermo ESCALAB 230XI. The SSA and pore size distribution were measured using nitrogen adsorption isotherms with the help of ASAP 2020M (Micromeritics Instrument Corp., USA) at 77 K. The content of SnO_2 and carbons matrix were measured on TA instrument Q600 analyzer by thermal gravimetric analysis (TGA) from 25 to 800 °C.

2.4. Electrochemical measurements

A slurry was composed of mixed active materials, carbon black and polyvinylidene fluoride with a weight ratio of 75 : 15 : 10 and a small quantity of *N*-methyl-2-pyrrolidinone (NMP). 1 M $LiPF_6$ dissolved in EC and DMC (1 : 1 by volume) was served as the electrolyte for LIBs and LICs. The obtained electrodes were coated onto a stainless steel foil and dried overnight at 80 °C. For LIB, electrochemical properties of anode materials were tested by 2032-type coin half-cells configuration with lithium metal foil as counter electrode.

Hybrid LICs were assembled using different weight proportions of pre-lithiated SnO_2/PCN anode to PCN cathode (1 : 1, 1 : 2, 1 : 3 and 1 : 4). The pre-lithiated SnO_2/PCN electrode was pre-activated for three cycles of charge/discharge at 100 mA g^{-1} in a lithium half-cell with a voltage window of 0.01–3 V. Cycle

Voltammetry (CV) and electrochemical impedance spectroscopies (EIS) were recorded on a CHI660E electrochemical workstation. Galvanostatic Charge–Discharge (GCD) measurements were obtained using Land CT2001 battery tester. The energy density (E, W h kg^{-1}) and power density (P, W kg^{-1}) were calculated as follows:

$$V_{ave} = \frac{V_{max} + V_{min}}{2} \quad (1)$$
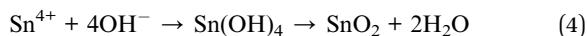
$$P = \frac{V_{ave} \times I}{m} \quad (2)$$

$$E = P \times t \quad (3)$$

where V_{max} and V_{min} refer to the maximum/minimum voltage at discharge (V). I represents the constant current density (A g^{-1}), m is mass of the active material (kg). t corresponds to discharge time (s).
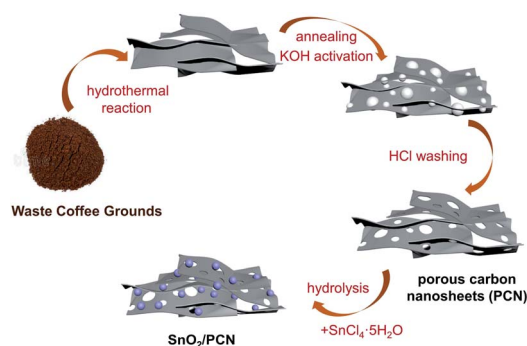
3. Results and discussion

3.1. Structure analysis

The synthesis process of SnO$_2$/PCN composite was demonstrated in Scheme 1. Firstly, Sn^{4+} ions released from precursor SnCl$_4$·5H$_2$O nucleates on PCN nanosheets activated by KOH and carbonized at high temperature. Meanwhile, the hierarchical interconnected carbon matrix has obvious porous structure, which can increase the SSA of SnO$_2$/PCN.[35,36] Oxygen-containing functional groups (such as –COOH or –OH) can be introduced to improve the absorption of Sn^{2+} or Sn^{4+} by KOH treatment.[37] Besides, the OH$^-$ ions from the hydrolysis of S$_2$O$_3$$^{2-}$ can combine with Sn^{4+} slowly. With the increase of hydrothermal reaction temperature, Sn^{4+} ions can hydrolyze into Sn(OH)$_4$, and then transform into SnO$_2$ nanoparticles.

$$Sn^{4+} + 4OH^- \rightarrow Sn(OH)_4 \rightarrow SnO_2 + 2H_2O \quad (4)$$

The detailed morphologies and microstructures of synthesized samples were observed by SEM and TEM. After activation and annealing of coffee grounds under nitrogen atmosphere, PCN appears a sheet-like structure with large and interconnected network, as shown in Fig. 1a and S1a.† While bare

Scheme 1 Schematic diagram of the synthesis process of SnO$_2$/PCN.

SnO$_2$ aggregated severely, it is unfavorable to the transportation of lithium ion and electron (Fig. 1c). With the combination of PCN and SnO$_2$, SnO$_2$ nanoparticles are uniformly anchored on the PCN frame without changing the sheet-like structure (Fig. 1b and S1b†). The crosslinked PCN network plays a positive role in improving the electrical conductivity and structural stability, and preventing SnO$_2$ from aggregation and pulverization during repeatedly charge–discharge process. TEM image of SnO$_2$/PCN hybrids (Fig. 1e) shows a lattice spacing 0.34 nm that can be indexed to (110) plane of rutile-type SnO$_2$, and proves the successful insertion of the SnO$_2$ nanoparticles.[38] The average diameter of crystallized SnO$_2$ is in the range of 2–4 nm. The mass content of SnO$_2$ in SnO$_2$/PCN composite is approximately 65.2 wt% calculated according to TGA in air flow (Fig. S2†).

The crystallographic structure of samples (SnO$_2$, SnO$_2$/PCN, and PCN) were collected through XRD as presented in Fig. 2a. Three distinguishable peaks are well assigned to the (110), (101) and (211) planes of rutile SnO$_2$ (JCPDS card no. 41-1445), suggesting high crystallinity and phase purity of the SnO$_2$ in SnO$_2$/PCN. Moreover, the peaks of SnO$_2$/PCN are a little broader than that of pure SnO$_2$, which could be deduced the hampered growth of SnO$_2$ nanocrystals by carbonaceous matrix. The grain size of 2.46 nm calculated by Scherrer equation is in accord with HRTEM results (Fig. 1e). Note that the broadened peaks of PCN at around 25° corresponds to the (002) plane of graphite, indicating an amorphous structure of PCN. Meanwhile, the interlayer space of (002) planes calculated from Bragg's Law is 0.359 nm larger than that of graphite (0.34 nm), signifying that PCN expanded interlayer spacing and amorphous structure, which can not only accelerate transportation of lithium ions into SnO$_2$, but also improve SnO$_2$/PCN electrode reversible capacities.[9,39] Raman spectra was carried out on PCN and SnO$_2$/PCN, as shown in Fig. 2b, manifesting two peaks at around 1350 cm^{-1} (disorder/defect-induced D band) and 1590 cm^{-1} (the graphitic G band) of carbonaceous materials.[40] The increased intensity ratio (I_D/I_G) for SnO$_2$/PCN (1.20) indicates more defects and disordered structure compared with PCN (0.89), which means decreased size of symmetric sp^2 C–C bonds domains resulting from the anchoring of SnO$_2$ nanoparticles on PCN.[23] In addition, no obvious characteristic peaks of SnO$_2$ can be detected from the SnO$_2$/PCN spectra, which may be attributed to the fact that SnO$_2$ nanoparticles are uniformly trapped in the void spaces or pores of PCN, or the SnO$_2$ crystalline size limited by PCN is too small to be detected.[41,42]

XPS shown in Fig. 2c, d and S3† were used to evaluate the elements composition and elemental valence state in the SnO$_2$/PCN hybrids. For high-resolution spectrum of Sn 3d spectrum of SnO$_2$/PCN show a pair of peaks of Sn 3d$_{5/2}$, Sn 3d$_{3/2}$ at 486.5 eV and 495.0 eV which are proved to be Sn^{4+} in Fig. 2c.[43,44] The peaks of O 1s are composed of three parts (Fig. 2d). A prominent peak located at 531.7 eV (Sn–O bonds), while the relatively weak peaks are concentrated at 532.7 eV (Sn–O–C) and 534.0 eV (C–O–C). The C 1s spectrum in Fig. S3a† can be indexed to the major C–C species (284.6 eV), O–C=O (284.8 eV), C–O/C–N (285.5 eV), Sn–O–C (286.4 eV) and O–C=O (289.2 eV), the presence of Sn–O–C indicates the tightly wrapping of SnO$_2$ by interconnected 2D porous network.[45,46] The N 1s spectrum of
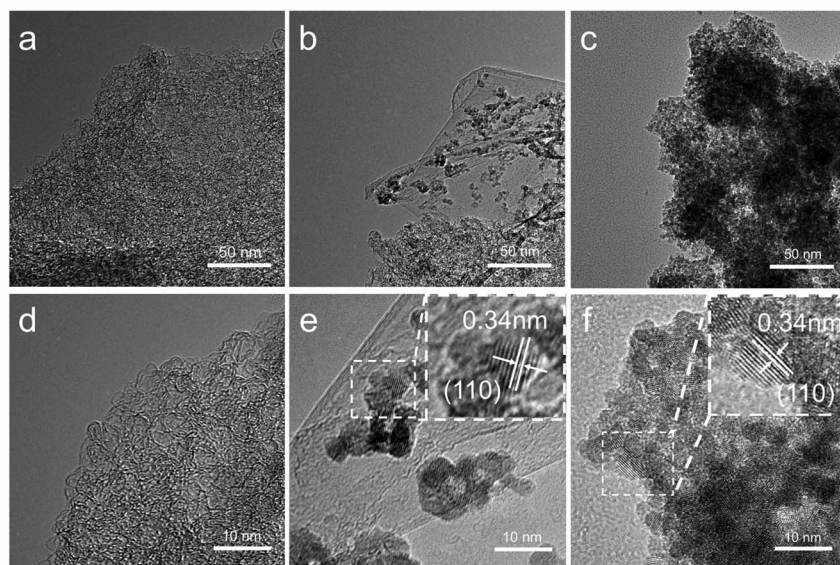
Fig. 1 TEM images of (a) PCN, (b) SnO_2/PCN and (c) pure SnO_2. HRTEM images of (d) PCN, (e) SnO_2/PCN and (f) pure SnO_2. Top inset image shows the lattices.
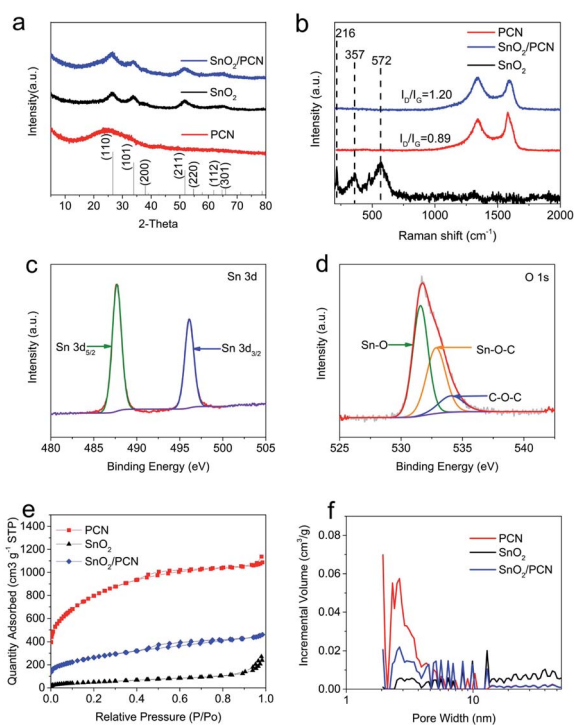

Fig. 2 (a) XRD patterns of PCN, SnO_2 and SnO_2/PCN. (b) Raman spectra of PCN, SnO_2, SnO_2/PCN. XPS spectra of (c) Sn 3d and (d) O 1s in the SnO_2/PCN. (e) Nitrogen adsorption–desorption isotherms of PCN, SnO_2 and SnO_2/PCN. (f) The corresponding pore distributions calculated by DFT.

SnO_2/PCN in Fig. S3b† is fitted as three peaks at 398.5, 400.0 and 401.5 eV, which are attributed to pyridinic-N, pyrrolic-N and graphitic-N, respectively.[47,48] The intrinsic nitrogen doping

derived from biomass precursor can tailor the intrinsic electron state of SnO_2/PCN, narrow the bandgap of SnO_2, thus further enhance the electron conductivity as well as shorten path of Li^+ diffusion.[49,50]

The evolution of SSA and porosity for SnO_2 and SnO_2/PCN were measured by nitrogen adsorption/desorption isotherms analysis. Fig. 2e depicts type-IV curves of SnO_2/PCN corresponding to the existence of micropores, mesopores and macropores. While SnO_2 has few porous structure, and it hardly uptakes N_2 even at high pressure.[51] The hierarchically porous structure of SnO_2/PCN originates from KOH activation and high-temperature decomposition of coffee grounds. The pore-size distribution calculated based on density functional theory (DFT) method shows that all samples present mesopores-dominated structure. In addition, the proportion of pore volume for mesopores shown in Fig. S4† are 84%, 97% and 89% for PCN, SnO_2 and SnO_2/PCN samples, which would facilitate the alkali metal storage and electrolyte infiltration. Meanwhile, abundant pores can also buffer the volume change of SnO_2 particle. The SSA and pore volume of PCN, SnO_2 and SnO_2/PCN are 2761 $m^2\ g^{-1}$ and 2.31 $cm^3\ g^{-1}$, 184 $m^2\ g^{-1}$ and 0.72 $cm^3\ g^{-1}$, 928 $m^2\ g^{-1}$ and 1.15 $cm^3\ g^{-1}$, respectively. Assuming that SnO_2 nanoparticles only distributed on the surface of PCN without filling in any pores, the reduction of SSA should be calculated simply by the weight ratio of SnO_2, and the pore size distribution should not change, which are evidently inconsistent with the above results. So it can be deduced that the decrease of SSA and pore volume in SnO_2/PCN is mainly due to the dispersion of SnO_2 nanoparticles in the micropores and mesopores of PCN. This structure also avoids the direct contact between SnO_2 and electrolyte during charging/discharging process, thereby improving the stability of the structure.

3.2. Electrochemical characterization in half-cells

The Li storage mechanism of SnO_2/PCN can be clarified through CV curves in Fig. 3a. As indicated by the first lithiation process, a reduction peak at around 1.0–1.5 V of SnO_2/PCN is ascribed to the generation of solid electrolyte interface (SEI) layer as well as conversion reaction of SnO_2 with Li^+ forming Sn and Li_2O. This conversion reaction is considered to be a decisive step because the coarsening of metallic Sn nanograins allows irreversible reaction of the electrode.[52,53] Another steep cathodic peak observed at around 0.1 V relates to the alloying Sn into Li_xSn ($0 \leq x \leq 4.4$) process and insertion of Li^+ into carbon layers and edge defects.[54] With cycles going on, one oxidation peak at 0.6 V appears, which is triggered by dealloying reaction of the Li_xSn to metallic Sn. Besides, an additional broad peak at around 1.2 V confirms the further oxidation of Sn to Sn^{4+} and Li_2O decomposition.[55,56] Note that except the first scan, the subsequent CV curves exhibit similar and overlapped shape, indicative of excellent cycling reversibility and stability during SnO_2/PCN lithiation/delithiation process. Meanwhile, at the same scanning rate, the integral area and peak current intensity under CV curve of SnO_2/PCN are larger than those of SnO_2 (Fig. S6a†), indicating that SnO_2/PCN has higher capacity and electrochemical activity.[57,58] Fig. 3b and S6b† demonstrate the GCD profiles SnO_2/PCN and SnO_2 at 0.1 A g^{-1}. The initial charge/discharge capacities of SnO_2/PCN electrode are 1021 and 2225 mA h g^{-1}, yielding a high initial coulombic efficiency (ICE) of 45.9% compared with those of SnO_2 electrode (38.5%). The inevitable formation of SEI film may be responsible for the irreversible capacity loss of both SnO_2 and SnO_2/PCN.[59] The improved ICE of SnO_2/PCN can be attributed to a stable SEI layer formation on the electrode by introducing carbon layers, the reduction in direct contact between SnO_2 and the electrolyte inhibits unfavorable side reactions further improving the ICE.[60,61] The rate performance of these samples under various

current densities were exhibited in Fig. 3c. As expected, the SnO_2/PCN presents the best rate capability and delivers reversible discharge capacities of 799, 644, 556, 496, 423 and 280 mA h g^{-1} at currents ranging from 0.1 to 5 A g^{-1}. While SnO_2 delivers negligible discharge capacity of 22.3 mA h g^{-1} at 5 A g^{-1}, it's unable to retain high capacity retention with inferior Li^+ storage. The cycle performance recorded at 1 A g^{-1} is shown in Fig. 3d, SnO_2/PCN shows better reversibility and cycling life performance than those of PCN and SnO_2 with the capacity can be maintained at 313 mA h g^{-1} after 500 loops (almost ten times of SnO_2). Whereas SnO_2 presents a drastic capacity loss (92.9%) after 500 cycles with poor capacity retention of only 38 mA h g^{-1}, which resulted from the aggregation and structure fracturing of SnO_2 nanoparticles derived by continuous volume change during the Li^+ insertion/extraction process. The corresponding ICE of SnO_2/PCN is 40% and quickly goes up to 98% without obvious changes during the subsequent cycles. The remarkable improvement of SnO_2/PCN cycle performance is related to the close combination of SnO_2 and conductive carbon network. Meanwhile, the carbon coating can improve the electronic conductivity, reduce the SnO_2 cluster effect and facilitate the Li^+/electron transportation.[62]

To verify the enhanced rate capability of as-prepared SnO_2/PCN electrode, EIS spectra are depicted in different cycles (Fig. S7a and c†), and the corresponding equivalent circuit models are shown in Fig. S7b and d.† A depressed semicircle in resultant EIS spectra is associated with the charge-transfer resistance (R_{ct}).[63,64] It can be found that after 500 cycles, the R_{ct} value of SnO_2 increased dramatically (263.4 Ω), while SnO_2/PCN maintains a low value of R_{ct} (57.7 Ω), which is almost one fifth of that of SnO_2, implying that PCN matrix is of great importance in enhancing the electron transportation at the electrolyte/electrode interface and improving the charge transfer efficiency. The slope of the linear part can be assigned to the solid-state ion diffusion impedance (Warburg impedance, R_w) from the surface to the interior of electrode. The R_w value of SnO_2/PCN is higher than that of SnO_2 electrode, which indicates that SnO_2/PCN has faster diffusion kinetics, better lithium ion reaction activity and good wettability for electrolyte.[65,66] As schematically shown in Fig. S7c,† the SnO_2/PCN electrode has smaller R_{ct} and R_w values compared to that of SnO_2 after 500 cycles, suggesting the better cycle reversibility of SnO_2/PCN electrode. Accordingly, due to the low intrinsic conductivity of SnO_2 electrode, both its electrochemical reversibility and Li^+ ions storage performance are limited.

To further investigate the electrochemistry kinetics and capacity contribution mechanism of the SnO_2/PCN hybrid, CV curves were collected. The CV curves of SnO_2/PCN in Fig. 4a show similar shapes and the anode/cathode peaks become wider as the scan rate increased to 1.0 mV s^{-1}, suggesting superior electrochemical reversibility and good rate performance of SnO_2/PCN electrode. Besides, the cathode peaks slightly shift to a lower potential since the decreased polarization of electrode material.[67] The peak current (i) and scan rate (v) obey the following eqn (5),[68,69]

$$i = av^b \quad (5)$$
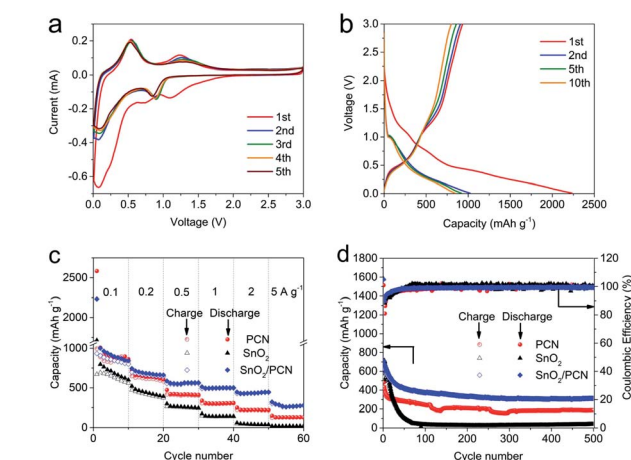

Fig. 3 (a) CV curves of SnO_2/PCN at a scan rate of 0.1 mV s^{-1}. (b) Galvanostatic charge/discharge profiles of SnO_2/PCN at 0.1 A g^{-1} for different selected cycles. (c) Rate performances of PCN, SnO_2 and SnO_2/PCN at various current densities. (d) Cycling performance and the related coulombic efficiency for PCN, SnO_2 and SnO_2/PCN at 1 A g^{-1} for 500 cycles.
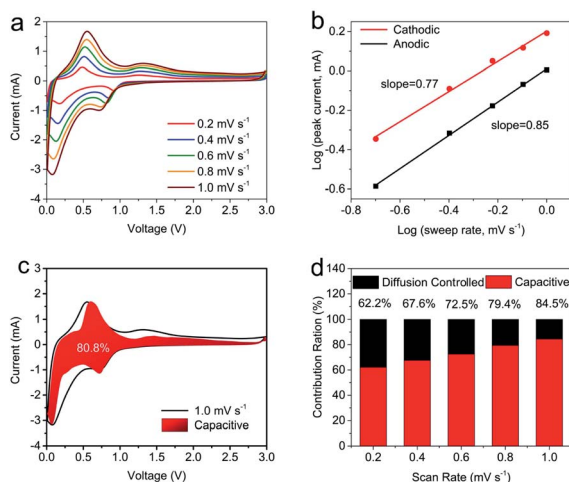
Fig. 4 (a) CV curves at different scan rates for SnO_2/PCN electrode. (b) Corresponding b values at cathodic and anodic peaks. (c) CV curve (1 mV s^{-1}) with the capacitive contribution as indicated. (d) Normalized contribution ratio of capacitive capacities at different scan rates for SnO_2/PCN.

The linear relationship ($b = 0.5$) reveals an ionic diffusion-dominated process whereas that of 1 refers to a totally surface-dominated capacitance process. The calculated b-values of SnO_2/PCN for the cathode and anode peaks are 0.77 and 0.85, indicating a hybrid Li$^+$ storage mechanism of SnO_2/PCN during the redox process.[70] In order to confirm percentage of capacitive contribution to entire capacity, the following equation can be used.

$$i = k_1v + k_2v^{1/2} \qquad (6)$$

in which the former and latter half of the formula on behalf of surface-driven pseudocapacitive behavior and diffusion-dominated processes, respectively. As depicted in Fig. 4c and d, the pseudocapacitive contribution of SnO_2/PCN accounts for 80.8% (the red region) at 1 mV s^{-1}. The ratios of capacitive control are enhanced correspondingly from 62.2% to 80.8% with the increase of scan speed. In view of the above results, it can be inferred that the superior Li$^+$ transport kinetics and good rate performance can be achieved for SnO_2/PCN primarily from its fascinating pseudocapacitive behaviors. Such fascinating pseudocapacitive behavior can be enhanced by SnO_2/PCN unique porous hierarchical architecture and large electrode–electrolyte contact area together with heteroatom N doping induced surface defects.[71]

As the cathode of the LIC, PCN features high SSA with porous structure. Compared with commercial active carbon cathode, the N doped PCN can provide numerous active sites with excellent anion double-layer adsorption/desorption performance and extremely fast charge/discharge rate performance. The electrochemical properties of PCN electrode were measured in a half-cell at a potential window of 3.0–4.5 V vs. Li/Li$^+$. Fig.-S8a† manifests the GCD curves of PCN at 0.1 A g^{-1}. The linear behavior reveals the electrical double layer capacitive behavior

of the PCN cathode with a reversible capacity about 44 mA h g^{-1}. Fig. S8b† demonstrates its good rate capability with the current density mounting from 0.1 to 10 A g^{-1}. Moreover, the PCN delivers decent cycle stability at 1 A g^{-1} with no obvious attenuation of capacity after 500 cycles (Fig. S8c†). PCN can be considered as a suitable cathode for LICs due to the above excellent electrochemical properties.

3.3. Electrochemical performance of lithium ion capacitor (LIC)

LICs were fabricated with SnO_2/PCN as anode and PCN as cathode in LiPF$_6$ electrolyte, denoted as SnO_2/PCN//PCN. During the charging process, Li$^+$ ions intercalate into SnO_2/PCN anode, while PF$_6^-$ ions are absorbed on the surface of hierarchical porous PCN cathode to store charge. A suitable voltage window of 1.0–4.0 V was determined to avoid electrolyte decomposition and facilitate the energy output of LICs.

In order to investigate synergistic effect of faradaic storage mechanisms (SnO_2/PCN anode) and adsorbing/desorbing reaction (PCN cathode), the CV and GCD curves of SnO_2/PCN//PCN with different weight proportions of anode-to-cathode (1 : 1, 1 : 2, 1 : 3 and 1 : 4) were investigated. The optimal mass ratio is 1 : 2 with the maximum electrochemical performance. As presented in Fig. 5a, CV curves based on these LICs slightly deviated from ideal rectangular shape, revealing the charge storage of SnO_2/PCN//PCN hybrid device is the combination of faradaic and non-faradaic energy storage mechanisms. Furthermore, the CV curves gradually deviate from the ideal capacitance shape along with the increasing mass ratio, which may be related to the deepening discharge voltage of the cathode. Similar variation tendency of CV and GCD curves under various current densities were shown in Fig. S9.† Even the current density at 200 mV s^{-1}, the CV shape is still near-rectangular, which suggests that hybrid SnO_2/PCN//PCN has high power capability. The GCD curves of the LICs are approximately symmetrical quasi-triangular with small voltage drop, which once again proves the remarkable power density contributed by the synergistic lithium storage mechanisms of the battery type anode and capacitive cathode.

The Ragone plot in Fig. 5c illustrates the high energy and power density of the SnO_2/PCN//PCN with different mass ratios. The optimized SnO_2/PCN//PCN hybrid device delivers excellent energy output over a wide power range: 138 W h kg^{-1} at 416 W kg^{-1} and 51 W h kg^{-1} at 53 kW kg^{-1}. The optimized SnO_2/PCN//PCN are superior to the recent representative LICs systems such as Zr-MOF//AC, MnO@HCF//AC, h-V$_2$O$_3$@C//AC, CNF//PANi@CN, Ni$_2$P@N–C//AC (Fig. 5d, Table S1†).[72–80] The LICs with SnO_2/PCN anode and PCN capacitive cathode overcome intrinsic sluggish kinetics, the reasons can be summarized as follows: (1) the conductivity of SnO_2 is improved by N-doped PCN nanosheets, and the mesoporous-dominated structure is conductive to the penetration and migration of the electrolyte. (2) SnO_2 nanoparticles can not only inhibit the close packing of PCN nanosheets, but also shorten the length of Li$^+$/electron diffusion path; (3) the intrinsic heteroatom doped PCN cathode favors adsorption/desorption of electrolyte ions, which further
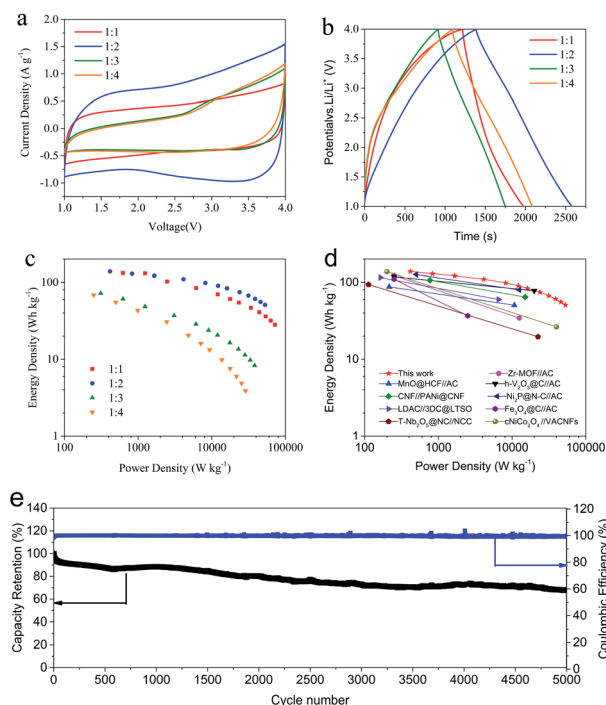
Fig. 5 Electrochemical properties of the SnO_2/PCN//PCN with different mass ratio of anode to cathode. (a) CV curves at the scan rates of 20 mV s^{-1}. (b) Galvanostatic charge/discharge profiles at 0.5 A g^{-1}. (c) Ragone plots. (d) Ragone plots in this work compared with other LICs. (e) Cycling performance of LIC with weight proportion of 1 : 2 at 5 A g^{-1}.

increases pseudo-capacitance and provides more active sites for lithium ions storage. The cycling stability of the SnO_2/PCN//PCN LIC was tested at 5 A g^{-1} after 5000 cycles in Fig. 5e, the LIC rendered 67% of retention with the CE about 100%, showing excellent cycle stability and reversibility.

To further evaluate the capacity decay mechanism of SnO_2/ PCN//PCN during cycling, EIS tests were measured after long cycling. The resultant EIS spectra and equivalent circuit diagram are displayed in Fig. S10a and b.† The slope is close to 90° in the low frequency region, which is mainly related to the capacitance behavior of SnO_2/PCN//PCN. The as-prepared SnO_2/ PCN//PCN shows a decreased R_{ct} value (varied from 12.6 Ω to 7.8 Ω after 5000 cycles) corresponding to the reduced semicircle radius. This phenomenon is owing to the slow activation of electrode.[23] However, the linear slope decreased after 5000 cycles, which is related to the capacity decay caused by the degradation of active materials, the continuous formation and deformation of charge–discharge products as well as the depletion of electrolyte.[70]

4. Conclusions

In summary, a composite material of SnO_2 nanoparticles anchored on biomass-derived PCN nanosheets was successfully synthesized by low-cost method. The SnO_2/PCN composite with favorable nanostructure has remarkable Li$^+$ storage performance and displays the high reversible capacity of 799 mA h g^{-1}

at 0.1 A g^{-1}, super rate performance of 280 mA h g^{-1} even at 5 A g^{-1} as well as excellent long-term cyclability over 500 cycles of 313 mA h g^{-1} at 1 A g^{-1}. Based on the synergistic effect between the hierarchical porous conductive network and the well dispersed SnO_2 nanoparticles, SnO_2/PCN has obvious pseudo-capacitive behavior. In addition, The LIC with SnO_2/ PCN anode and PCN cathode delivers superior combination of high energy and power characteristics, reaching 138 W h kg^{-1} and 53 kW kg^{-1} as well as excellent cyclability upon extremely long cycling. This work offers a potential way for large-scale production in stationary energy storage systems.

Conflicts of interest

There are no conflicts to declare.

Acknowledgements

Notes and references

1 H. Wang, C. Zhu, D. Chao, Q. Yan and H. J. Fan, *Adv. Mater.*, 2017, **29**, 1702093.

2 C. Liu, M. Zhang, X. Zhang, B. Wan, X. Li, H. Gou, Y. Wang, F. Yin and G. Wang, *Small*, 2020, 2004457.

3 W. Fu, E. Zhao, R. Ma, Z. Sun, Y. Yang, M. Sevilla, A. B. Fuertes, A. Magasinski and G. Yushin, *Adv. Energy Mater.*, 2020, **10**, 1902993.

4 D. Yang, Q. Zhao, L. Huang, B. Xu, N. A. Kumar and X. S. Zhao, *J. Mater. Chem. A*, 2018, **6**, 14146–14154.

5 G. Zhu, T. Chen, L. Wang, L. Ma, Y. Hu, R. Chen, Y. Wang, C. Wang, W. Yan and Z. Tie, *Energy Storage Mater.*, 2018, **14**, 246–252.

6 Z. Zhou, X. Zhou, M. Zhang, S. Mu, Q. Liu and Y. Tang, *Small*, 2020, **16**, 2003174.

7 H. Tan, X. Lin, J. Huang, J. Huang, M. Shi, X. Du and B. Zhang, *Nanoscale*, 2019, **11**, 11445–11450.

8 K. Share, A. P. Cohn, R. Carter, B. Rogers and C. L. Pint, *ACS Nano*, 2016, **10**, 9738–9744.

9 B. Yang, J. Chen, L. Liu, P. Ma, B. Liu, J. Lang, Y. Tang and X. Yan, *Energy Storage Mater.*, 2019, **23**, 522–529.

10 T. Liu, B. Lee, M. J. Lee, J. Park, Z. Chen, S. Noda and S. W. Lee, *J. Mater. Chem. A*, 2018, **6**, 3367–3375.

11 F. Wang, J. Huang, Y. Yang, L. Xu and L. Yu, *Ind. Eng. Chem. Res.*, 2019, **59**, 1025–1029.

12 X. Mao, P. Li, T. Li, M. Zhao, C. Chen, J. Liu, Z. Wang and L. Yu, *Chin. Chem. Lett.*, 2020, **31**, 3276–3278.

13 H. Cao, Y. Yang, X. Chen, J. Liu, C. Chen, S. Yuan and L. Yu, *Chin. Chem. Lett.*, 2020, **31**, 1887–1889.

14 T. Shang, Y. Xu, P. Li, J. Han, Z. Wu, Y. Tao and Q.-H. Yang, *Nano energy*, 2020, **70**, 104531.

15 Q. Jin, W. Li, K. Wang, H. Li, P. Feng, Z. Zhang, W. Wang and K. Jiang, *Adv. Funct. Mater.*, 2020, **30**, 1909907.

16 Y. Gao, S. Zheng, H. Fu, J. Ma, X. Xu, L. Guan, H. Wu and Z.-S. Wu, *Carbon*, 2020, **168**, 701–709.

17 L. Jin, C. Shen, A. Shellikeri, Q. Wu, J. Zheng, P. Andrei, J.-G. Zhang and J. P. Zheng, *Energy Environ. Sci.*, 2020, **13**, 2341–2362.

18 S. Zhao, C. D. Sewell, R. Liu, S. Jia, Z. Wang, Y. He, K. Yuan, H. Jin, S. Wang and X. Liu, *Adv. Energy Mater.*, 2020, **10**, 1902657.

19 S. Fu, Q. Yu, Z. Liu, P. Hu, Q. Chen, S. Feng, L. Mai and L. Zhou, *J. Mater. Chem. A*, 2019, **7**, 11234–11240.

20 B. Jia, W. Chen, J. Luo, Z. Yang, L. Li and L. Guo, *Adv. Mater.*, 2020, **32**, 1906582.

21 C. Wang, L. Zhang, M. Al-Mamun, Y. Dou, P. Liu, D. Su, G. Wang, S. Zhang, D. Wang and H. Zhao, *Adv. Energy Mater.*, 2019, **9**, 1900909.

22 H. Qiu, L. Zhao, M. Asif, X. Huang, T. Tang, W. Li, T. Zhang, T. Shen and Y. Hou, *Energy Environ. Sci.*, 2020, **13**, 571–578.

23 L. Fan, X. Li, B. Yan, J. Feng, D. Xiong, D. Li, L. Gu, Y. Wen, S. Lawes and X. Sun, *Adv. Energy Mater.*, 2016, **6**, 1502057.

24 T. Liang, R. Hu, H. Zhang, H. Zhang, H. Wang, Y. Ouyang, J. Liu, L. Yang and M. Zhu, *J. Mater. Chem. A*, 2018, **6**, 7206–7220.

25 A.-Y. Kim, R. E. A. Ardhi, G. Liu, J. Y. Kim, H.-J. Shin, D. Byun and J. K. Lee, *Carbon*, 2019, **153**, 62–72.

26 X. Zhou, L. Yu and X. W. Lou, *Adv. Energy Mater.*, 2016, **6**, 1600451.

27 Y. Cheng, S. Wang, L. Zhou, L. Chang, W. Liu, D. Yin, Z. Yi and L. Wang, *Small*, 2020, 2000681.

28 Y. Cheng, J. Huang, H. Qi, L. Cao, J. Yang, Q. Xi, X. Luo, K. Yanagisawa and J. Li, *Small*, 2017, **13**, 1700656.

29 S. Ding, J. S. Chen and X. W. Lou, *Adv. Funct. Mater.*, 2011, **21**, 4120–4125.

30 K. Zhao, L. Zhang, R. Xia, Y. Dong, W. Xu, C. Niu, L. He, M. Yan, L. Qu and L. Mai, *Small*, 2016, **12**, 588–594.

31 H. Xu, J. Chen, D. Wang, Z. Sun, P. Zhang, Y. Zhang and X. Guo, *Carbon*, 2017, **124**, 565–575.

32 C. Gao, Z. Jiang, P. Wang, L. R. Jensen, Y. Zhang and Y. Yue, *Nano Energy*, 2020, 104868.

33 Y. Li, Q. Meng, J. Ma, C. Zhu, J. Cui, Z. Chen, Z. Guo, T. Zhang, S. Zhu and D. Zhang, *ACS Appl. Mater. Interfaces*, 2015, **7**, 11146–11154.

34 A. A. Fazil, J. U. Bhanu, A. Amutha, S. Joicy, N. Ponpandian, S. Amirthapandian, B. Panigrahi and P. Thangadurai, *Microporous Mesoporous Mater.*, 2015, **212**, 91–99.

35 J. Wang and S. Kaskel, *J. Mater. Chem.*, 2012, **22**, 23710–23725.

36 S. N. Talapaneni, J. H. Lee, S. H. Je, O. Buyukcakir, T. w. Kwon, K. Polychronopoulou, J. W. Choi and A. Coskun, *Adv. Funct. Mater.*, 2017, **27**, 1604658.

37 H. Zhang, H. Song, X. Chen, J. Zhou and H. Zhang, *Electrochim. Acta*, 2012, **59**, 160–167.

38 Y. Cheng, J. Huang, H. Qi, L. Cao, J. Yang, Q. Xi, X. Luo, K. Yanagisawa and J. Li, *Small*, 2017, 1700656.

39 P. Lu, Y. Sun, H. Xiang, X. Liang and Y. Yu, *Adv. Energy Mater.*, 2018, 8.

40 C. Yang, Y. Zhang, J. Zhou, C. Lin, L. Fan and K. Wang, *J. Mater. Chem. A*, 2018, **6**, 8039–8046.

41 S. J. R. Prabakar, Y. H. Hwang, E. G. Bae, S. Shim, D. Kim, M. S. Lah, K. S. Sohn and M. Pyo, *Adv. Mater.*, 2013, **25**, 3307–3312.

42 W. Mao, W. Yue, Z. Xu, S. Chang, Q. Hu, F. Pei, X. Huang, J. Zhang, D. Li and G. Liu, *ACS Nano*, 2020, **14**, 4741–4754.

43 Z. Chen, D. Yin and M. Zhang, *Small*, 2018, **14**, 1703818.

44 G. D. Park, J. K. Lee and Y. C. Kang, *Adv. Funct. Mater.*, 2017, **27**, 1603399.

45 X. Min, B. Sun, S. Chen, M. Fang, X. Wu, Y. g. Liu, A. Abdelkader, Z. Huang, T. Liu and K. Xi, *Energy Storage Mater.*, 2019, **16**, 597–606.

46 W. Chen, K. Song, L. Mi, X. Feng, J. Zhang, S. Cui and C. Liu, *J. Mater. Chem. A*, 2017, **5**, 10027–10038.

47 B. Wang, Z. Deng, Y. Xia, J. Hu, H. Li, H. Wu, Q. Zhang, Y. Zhang, H. Liu and S. Dou, *Adv. Energy Mater.*, 2020, **10**, 1903119.

48 Y. Zhang, L. Tao, C. Xie, D. Wang, Y. Zou, R. Chen, Y. Wang, C. Jia and S. Wang, *Adv. Mater.*, 2020, **32**, 1905923.

49 D. Li, J. Li, J. Cao, X. Fu, L. Zhou and W. Han, *Sustainable Energy Fuels*, 2020, **4**, 5732–5738.

50 X. Shi, J. Zhang, Q. Yao, R. Wang, H. Wu, Y. Zhao and L. Guan, *J. Mater. Chem. A*, 2020, **8**, 8002–8009.

51 J. Chen, S. Li, V. Kumar and P. S. Lee, *Adv. Energy Mater.*, 2017, **7**, 1700180.

52 R. Hu, H. Zhang, Z. Lu, J. Liu, M. Zeng, L. Yang, B. Yuan and M. Zhu, *Nano Energy*, 2018, **45**, 255–265.

53 J. H. Chang, J. Y. Cheong, J. M. Yuk, C. Kim, S. J. Kim, H. K. Seo, I.-D. Kim and J. Y. Lee, *ACS Omega*, 2017, **2**, 6329–6336.

54 G. Ferraresi, C. Villevieille, I. Czekaj, M. Horisberger, P. Novák and M. El Kazzi, *ACS Appl. Mater. Interfaces*, 2018, **10**, 8712–8720.

55 Q. Wu, Q. Shao, Q. Li, Q. Duan, Y. Li and H.-g. Wang, *ACS Appl. Mater. Interfaces*, 2018, **10**, 15642–15651.

56 I. Sultana, T. Ramireddy, M. M. Rahman, Y. Chen and A. M. Glushenkov, *Chem. Commun.*, 2016, **52**, 9279–9282.

57 C. Yang, F. Lv, Y. Zhang, J. Wen, K. Dong, H. Su, F. Lai, G. Qian, W. Wang and A. Hilger, *Adv. Energy Mater.*, 2019, **9**, 1902674.

58 R. Hu, D. Chen, G. Waller, Y. Ouyang, Y. Chen, B. Zhao, B. Rainwater, C. Yang, M. Zhu and M. Liu, *Energy Environ. Sci.*, 2016, **9**, 595–603.

59 W. Zhao, X. Ma, L. Gao, Y. Li, G. Wang and Q. Sun, *Carbon*, 2020, **167**, 736–745.

60 Y. Zhao, L. P. Wang, S. Xi, Y. Du, Q. Yao, L. Guan and Z. J. Xu, *J. Mater. Chem. A*, 2017, **5**, 25609–25617.

61 X. Li, X. Sun, X. Hu, F. Fan, S. Cai, C. Zheng and G. D. Stucky, *Nano Energy*, 2020, 105143.

62 Q. Li, L. Li, P. Wu, N. Xu, L. Wang, M. Li, A. Dai, K. Amine, L. Mai and J. Lu, *Adv. Energy Mater.*, 2019, **9**, 1901153.

63 X. Deng, Z. Wei, C. Cui, Q. Liu, C. Wang and J. Ma, *J. Mater. Chem. A*, 2018, **6**, 4013–4022.

64 C. Yang, J. Feng, F. Lv, J. Zhou, C. Lin, K. Wang, Y. Zhang, Y. Yang, W. Wang and J. Li, *Adv. Mater.*, 2018, **30**, 1800036.

65 H. Qiu, K. Zhu, H. Li, T. Li, T. Zhang, H. Yue, Y. Wei, F. Du, C. Wang and G. Chen, *Carbon*, 2015, **87**, 365–373.

66 J.-Y. Li, X.-L. Wu, X.-H. Zhang, H.-Y. Lü, G. Wang, J.-Z. Guo, F. Wan and R.-S. Wang, *Chem. Commun.*, 2015, **51**, 14848–14851.

67 D. Cai, B. Liu, D. Zhu, D. Chen, M. Lu, J. Cao, Y. Wang, W. Huang, Y. Shao and H. Tu, *Adv. Energy Mater.*, 2020, **10**, 1904273.

68 Y. Ma, Y. Ma, D. Bresser, Y. Ji, D. Geiger, U. Kaiser, C. Streb, A. Varzi and S. Passerini, *ACS Nano*, 2018, **12**, 7220–7231.

69 W. Chen, X. Zhang, L. Mi, C. Liu, J. Zhang, S. Cui, X. Feng, Y. Cao and C. Shen, *Adv. Mater.*, 2019, **31**, 1806664.

70 J. Liu, J. Wang, C. Xu, H. Jiang, C. Li, L. Zhang, J. Lin and Z. X. Shen, *Adv. Sci.*, 2018, **5**, 1700322.

71 F. Xu, Y. Zhai, E. Zhang, Q. Liu, G. Jiang, X. Xu, Y. Qiu, X. Liu, H. Wang and S. Kaskel, *Angew. Chem., Int. Ed.*, 2020, **59**, 19460–19467.

72 W. Yan, J. Su, Z. M. Yang, S. Lv, Z. Jin and J. L. Zuo, *Small*, 2020, 2005209.

73 Z.-Y. Chen, B. He, D. Yan, X.-F. Yu and W.-C. Li, *J. Power Sources*, 2020, **472**, 228501.

74 Z. Mao, H. Wang, D. Chao, R. Wang, B. He, Y. Gong and H. J. Fan, *Small*, 2020, **16**, 2001950.

75 C. Han, J. Tong, X. Tang, D. Zhou, H. Duan, B. Li and G. Wang, *ACS Appl. Mater. Interfaces*, 2020, **12**, 10479–10489.

76 H. Yuan, M. Wu, J. Zheng, Z. G. Chen, W. Zhang, J. Luo, C. Jin, O. Sheng, C. Liang and Y. Gan, *Adv. Funct. Mater.*, 2019, **29**, 1809051.

77 L. Jin, R. Gong, W. Zhang, Y. Xiang, J. Zheng, Z. Xiang, C. Zhang, Y. Xia and J. P. Zheng, *J. Mater. Chem. A*, 2019, **7**, 8234–8244.

78 C. Han, L. Xu, H. Li, R. Shi, T. Zhang, J. Li, C.-P. Wong, F. Kang, Z. Lin and B. Li, *Carbon*, 2018, **140**, 296–305.

79 R. Bi, N. Xu, H. Ren, N. Yang, Y. Sun, A. Cao, R. Yu and D. Wang, *Angew. Chem.*, 2020, **132**, 4895–4898.

80 C.-F. Cheng, X. Li, K. Liu, F. Zou, W.-Y. Tung, Y.-F. Huang, X. Xia, C.-L. Wang, B. D. Vogt and Y. Zhu, *Energy Storage Mater.*, 2019, **22**, 265–274.